

Impacts of Hurricane Irma (2017) on ocean transport processes

Thomas Dobbelaere^{a,*}, Milan Curcic^b, Matthieu le Hénaff^{c,d}, Emmanuel Hanert^{a,e}

^a*Eath and Life Institute (ELI), UCLouvain, Louvain-la-Neuve, Belgium*

^b*Rosenstiel School of Marine and Atmospheric Sciences (RSMAS), University of Miami, Coral Gables, Florida, USA*

^c*Cooperative Institute for Marine and Atmospheric Studies (CIMAS), University of Miami, Miami, Florida, USA*

^d*Atlantic Oceanographic and Meteorological Laboratory (AOML), NOAA, Miami, Florida, USA*

^e*Institute of Mechanics, Materials and Civil Engineering (IMMC), UCLouvain, Louvain-la-Neuve, Belgium*

Abstract

Tropical cyclones are becoming more intense and more frequent. Their effect is particularly acute in coastal areas where they cause extensive damage leading to an influx of debris, sediments and waste to the sea. However, most coastal ocean models do not represent heavy-wind transport processes correctly as they do not couple the hydrodynamics with the wind-generated waves. This may lead to significant errors in simulations of tropical cyclones. Here, we investigate current-wave interactions during a major hurricane and assess their impact on transport processes. We do that by coupling the unstructured-mesh coastal ocean model SLIM with the spectral wave model SWAN, and applying it to the Florida Reef Tract during Hurricane Irma (September 17). We show that the coupled model successfully reproduces the wave behavior, the storm surge and the ocean currents during the passage of the hurricane. We then use the coupled and uncoupled wave-current model to simulate the transport

*Corresponding author

Email address: thomas.dobbelaere@uclouvain.be (Thomas Dobbelaere)

of passive drifters. We show that the wave radiation stress gradient alone can lead to changes of up to 1 m/s in the modeled currents, which in turn leads to differences of up to 5 km in the position of drifting material over the duration of the hurricane. The Stokes drift however appears to be up to 4 times more intense and should thus be considered in priority. Wave-current interactions therefore strongly impact the transport of drifting material such as sediments and debris in the aftermath of a hurricane. They should thus be taken into account in order to correctly assess its overall impact.

Keywords: Hurricane, Ocean transport, Wave-current interactions

1. Introduction

Tropical cyclones are becoming more intense and more frequent (Bhatia et al., 2019; Kossin et al., 2020). This increase is likely due to climate change and will probably continue in the future (Knutson et al., 2020). However, estimating the impact of tropical cyclones on the coastal ocean circulation remains a challenge. Understanding wave-current interactions and representing their impact on coastal ocean transport processes is central to many coastal activities such as dredging, erosion management, Oil & Gas, search and rescue, and insurance (Bever and MacWilliams, 2013; Li and Johns, 1998; Breivik et al., 2013). All these activities require wave-current models to predict the impact of tropical cyclones on the coastal circulation and on water-level changes.

Wave-current interactions during a cyclone are highly nonlinear and vary significantly in space and time (Wu et al., 2011). Wave-induced currents are generated by wave radiation stress gradients (Longuet-Higgins, 1970), affecting water levels near shorelines and wave breaking points (Longuet-Higgins and Stewart, 1964). Changes in water levels and currents, in turn, affect the motion and evolution of the waves (Sikirić et al., 2013). Coupled wave-current models hence require the calculation of the full directional wave spectrum in order to correctly reproduce the dynamics of wind-driven surface

waves. This is usually achieved by spectral wave models, which describe the evolution of the wave energy spectrum. As of today, the most popular spectral wave models are WAM (WAMDI Group, 1988), SWAN (Booij et al., 1999), and WAVEWATCH III (Tolman et al., 2009). Among these models, SWAN is more fitted to coastal applications, as it represents depth-induced wave breaking and triad wave-wave interactions, while implementing numerical techniques adapted to small-scale, shallow water regions (Booij et al., 1999).

Coastal oceans are characterized by the complex topography of the coastline and the presence of islands, reefs and artificial structures. Traditional structured-grid models lack the flexibility to simulate near-shore processes at a sufficiently small scale. Instead, unstructured-mesh models easily adapt to the topography and are hence better suited to coastal processes (Fringer et al., 2019). Capturing the impact of the topography on wave interactions becomes even more important in the case of tropical cyclones. Heavy winds generate large wind-waves and disturb ocean conditions (Liu et al., 2020) by causing coastal upwellings on continental shelves (Smith, 1982) and inducing strong currents, waves and storm surges in nearshore and coastal regions (Dietrich et al., 2010; Weisberg and Zheng, 2006).

The transport of drifting objects or substances that are locally released is often best represented by a Lagrangian individual-based model. Such an approach is routinely used to model the dispersal of larvae, pollutants, sediments and many other tracers (e.g. Le Hénaff et al., 2012; Liubartseva et al., 2018; Figueiredo et al., 2013; Frys et al., 2020). Although some transport models take the impact of waves into account by adding a Stokes drift velocity, *i.e.* the net drift of a floating particle in the direction of the wave propagation (Van Den Bremer and Breivik, 2018), to the Eulerian currents, they usually neglect the wave-induced currents. Such practice is reasonable in fair weather, when wave-induced forces exerted on currents are relatively small, but may lead to significant errors during storm conditions (Röhrs et al., 2012; Curcic et al., 2016).

51 The objective of this study is therefore to assess the importance of wave-
52 current interactions during a tropical cyclone. We investigate the transport
53 of drifting particles on the Florida shelf during Hurricane Irma, one of the
54 strongest and costliest tropical cyclones on record in the Atlantic Basin (Xian
55 et al., 2018), which made landfall in Florida in September 2017. To do
56 that, we developed an unstructured-mesh coupled wave-current model of
57 South Florida to simulate the ocean circulation under hurricane conditions.
58 Both modeled currents and waves were validated against field measurements
59 and then used to simulate the transport of drifting material in the Florida
60 Keys and the Florida inner shelf. Model outputs were then compared with
61 uncoupled simulation results in order to assess the impact of wave-induced
62 forces and Stokes drift on the modeled currents and transports.

63 **2. Methods**

64 *2.1. Study area and observational data*

65 The large-scale ocean circulation around South Florida is dominated by
66 the Florida Current (FC), which originates from the Loop Current (LC) where
67 it enters the Florida Straits from the Gulf of Mexico, and, downstream, forms
68 the Gulf Stream. The FC is a major western boundary current characterized
69 by spatial variability and meandering, associated with the presence of cyclonic
70 eddies between the core of the current and the complex reef topography
71 of the Florida Reef Tract (FRT) (Lee et al., 1995; Kourafalou and Kang,
72 2012). The variability of the FC extends over a large range of spatial and
73 temporal scales, with periods of 30-70 days in the Lower Keys (Lee et al., 1995)
74 and shorter periods of 2-21 days in the Upper Keys (Lee and Mayer, 1977),
75 and exhibits significant seasonal and interannual cycles (Johns and Schott,
76 1987; Lee and Williams, 1988; Schott et al., 1988). Circulation on the West
77 Florida Shelf (WFS), on the other hand, is forced by local winds and tidal
78 fluctuations (Lee and Smith, 2002; Liu and Weisberg, 2012). Furthermore,
79 due to its location relative to the warm waters of the North Atlantic, Florida

80 is particularly vulnerable to tropical cyclones. On average, the state gets
81 hit by a hurricane every two years and strong hurricanes, some of which are
82 among the most destructive on record, strike Florida on average once every
83 four years (Malmstadt et al., 2009).

84 The state of the ocean around Florida is monitored by an extensive
85 array of tide gauges, current meters and buoys. In this study, we used sea
86 surface elevation measurements from the National Oceanic and Atmospheric
87 Administrations (NOAA) Tides and Currents dataset. These measurements
88 were taken at four locations: two in the Florida Keys (Key West and Vaca
89 Key); one on the East coast of Florida (Virginia Key); and one on the West
90 coast (Naples). For the currents, we used ADCP measurements from the
91 University of South Florida's College of Marine Science's (USF/CMS) Coastal
92 Ocean Monitoring and Prediction System (COMPS) for the WFS (Weisberg
93 et al., 2009). More specifically, we used measurements from moorings C10,
94 C12 and C13, respectively located at the 25, 50, and 50 m isobaths of the
95 WFS (Liu et al., 2020). Finally, for the waves, we used measurements from
96 four buoys of the NOAA's National Data Buoy Center (NDBC); two on
97 Florida's eastern shelf and two on the WFS. The locations of all measurement
98 stations are shown in Fig. 1A,C.

99 *2.2. Wind and atmospheric pressure during Hurricane Irma*

100 Hurricane Irma made landfall in Florida on 10 September 2017 as a
101 category 3 hurricane, first at Cudjoe Key (Florida Keys) and later on Marco
102 Island, south of Naples (see hurricane track in Fig. 1). It then weakened to a
103 category 2 hurricane as it moved further inland (Pinelli et al., 2018). The
104 storm damaged up to 75% of the buildings at its landfall point in the Florida
105 Keys, making it one of the strongest and costliest hurricanes on record in the
106 Atlantic basin (Xian et al., 2018; Zhang et al., 2019). The strongest reported
107 wind speed was 50 m/s on Marco Island while the highest recorded storm
108 surge was 2.3 m, although larger wind speed likely occurred in the Florida
109 Keys (Pinelli et al., 2018). To reproduce the wind profile of Irma in our model,

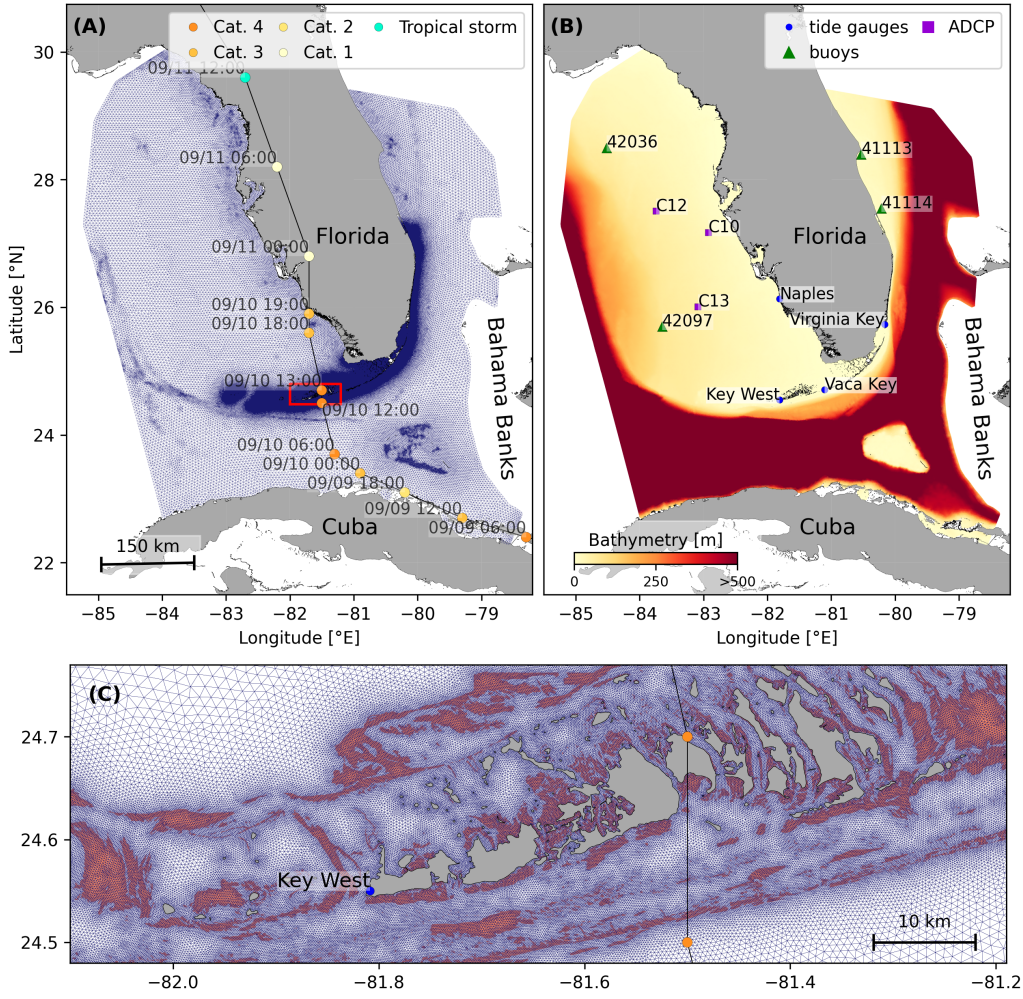


Fig. 1: (A) Mesh of the computational domain with the trajectory of Irma. The category of the hurricane is given by the Saffir-Simpson color scale. (B) Bathymetry of the domain with the location of stations used for the validation of the model outputs. (C) Close up view of the Lower Keys area, where the mesh resolution reaches 100 m near reefs (shown in dark orange) and islands (highlighted in dark grey)

we used high-resolution H*Wind wind fields (Powell et al., 1998). As these data represent 1-min averaged wind speeds, we multiplied them by a factor 0.93 to obtain 10-min averaged wind speeds (Harper et al., 2010), which are more consistent with the time step of our model. Furthermore, H*Wind wind profiles did not cover the whole model extent during the passage of the hurricane and were thus blended within coarser wind field extracted from ECMWF ERA-5 datasets (Fig. 2A). The pressure field during the passage of Hurricane Irma was also reconstructed using ERA-5 data. However, the coarse resolution of the dataset smoothes out the depression at the center of the hurricane, leading to an underestimation of the pressure gradient (Fig. 2B). To better capture the central depression of Irma, we therefore built a hybrid pressure field using the position and the minimal pressure of the core of the hurricane based on its track as recorded in the HURDAT 2 database (Landsea and Franklin, 2013). Based on this information, the hybrid pressure field was constructed by combining an idealized Holland pressure profile (Lin and Chavas, 2012) within the radius of maximum wind speed of Irma (Knaff et al., 2018) with ERA-5 pressure field. The transition from the Holland profile to ERA-5 data outside the radius of maximum wind speed data was performed using a smooth step function (Fig. 2).

2.3. Hydrodynamic model

Ocean currents generated during hurricane Irma around South Florida were modeled using the 2D barotropic version of the unstructured-mesh coastal ocean model SLIM¹ (Lambrechts et al., 2008). The model mesh covers an area similar to the model extent of Dobbelaere et al. (2020), that includes the FRT but also the Florida Straits and part of the Gulf of Mexico (Figure 1). However, this area has been slightly extended northeastward and westward in order to include the NOAA-NDBC buoys. Furthermore, to withstand potential cell drying during the hurricane, we solved the conservative shallow

¹<https://www.slim-ocean.be>

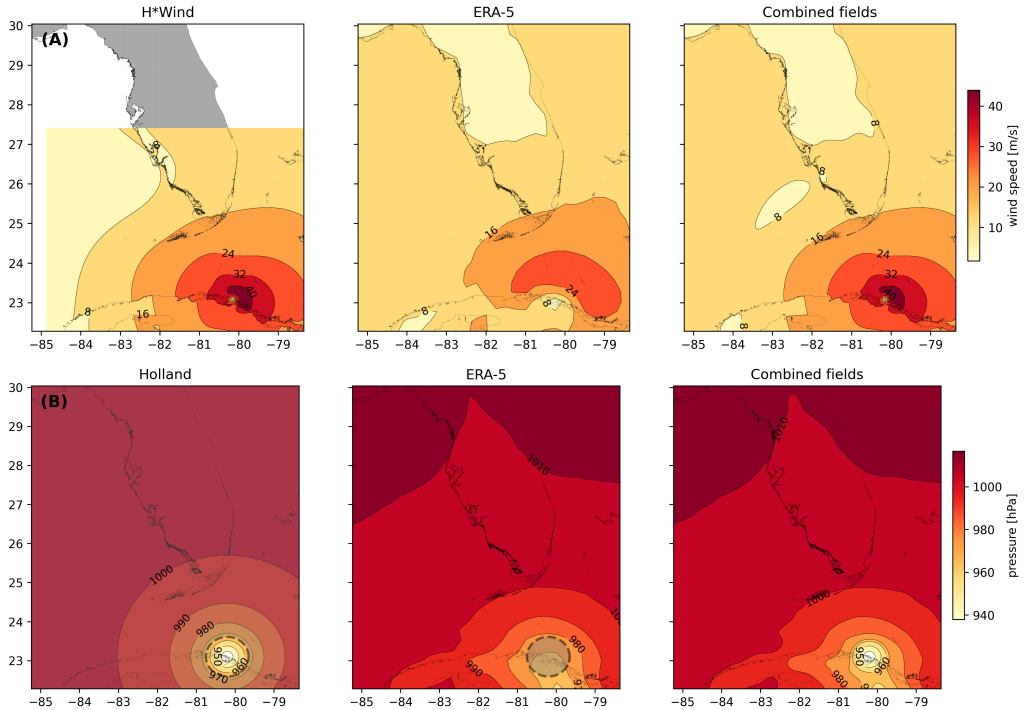


Fig. 2: Snapshot of the hybrid wind (A) and pressure (B) profiles constructed to capture the passage of Hurricane Irma at 1800 UTC on 9 September 2017. Wind profiles are obtained by combining high resolution H*Wind with coarser ERA-5 wind fields. The pressure field is built by combining the ERA-5 pressure field with an idealized Holland pressure profile based on the track of Irma in the HURDAT 2 database. Holland field was only used within the radius of maximum wind speed (dashed grey line) of the hurricane to capture its central depression.

₁₃₈ water equations with wetting-drying:

$$\begin{aligned} \frac{\partial H}{\partial t} + \nabla \cdot (\mathbf{U}) &= 0, \\ \frac{\partial \mathbf{U}}{\partial t} + \nabla \cdot \left(\frac{\mathbf{U}\mathbf{U}}{H} \right) + f\mathbf{e}_z \times \mathbf{U} &= \alpha g H \nabla(H - h) - \frac{1}{\rho} \nabla p_{\text{atm}} + \frac{1}{\rho} \boldsymbol{\tau}_s \\ &\quad + \nabla \cdot (\nu \nabla \mathbf{U}) - \frac{C_b}{H^2} |\mathbf{U}| \mathbf{U} + \gamma (\mathbf{U}_{\text{ref}} - \mathbf{U}), \end{aligned} \quad (1)$$

₁₃₉ where H is the water column height and \mathbf{U} is the depth-averaged transport;
₁₄₀ f is the Coriolis coefficient; g is the gravitational acceleration; h is the
₁₄₁ bathymetry; α is a coefficient indicating whether the mesh element is wet
₁₄₂ ($\alpha = 1$) or dry ($\alpha = 0$) (Le et al., 2020); ν is the viscosity; C_b is the
₁₄₃ bulk bottom drag coefficient; p_{atm} is the atmospheric pressure; $\boldsymbol{\tau}_s$ is the
₁₄₄ surface stress, usually due to wind; and γ is a relaxation coefficient towards a
₁₄₅ reference transport \mathbf{U}_{ref} . As in Frys et al. (2020) and Dobbelaere et al. (2020),
₁₄₆ SLIM currents were gradually relaxed towards the operational Navy HYCOM
₁₄₇ product (GOMl0.04², Chassignet et al. (2007)) in regions where the water
₁₄₈ depth exceeds 50m.

₁₄₉ At very high wind speeds, the white cap is blown off the crest of the
₁₅₀ waves. This phenomenon, also known as spume, has been hypothesized to
₁₅₁ generate a layer of droplets that acts as a slip layer for the winds at the
₁₅₂ ocean-atmosphere interface (Holthuijsen et al., 2012). It causes a saturation
₁₅₃ of the wind drag coefficient for strong winds (Powell et al., 2003; Donelan
₁₅₄ et al., 2004; Curcic and Haus, 2020). We take this saturation effect into
₁₅₅ account by using the wind drag parameterization of Moon et al. (2007). In
₁₅₆ this parameterization, the drag coefficient C_d depends on the wind speed at

²<https://www.hycom.org/data/goml0pt04>

₁₅₇ 10-m height U_{10} according to:

$$C_d = \kappa^2 \log \left(\frac{10}{z_0} \right)^{-2} \quad (2)$$

₁₅₈ where κ is the von Karman constant and z_0 is the roughness length expressed
₁₅₉ as:

$$z_0 = \begin{cases} \frac{0.0185}{g} u_*^2 & \text{if } U_{10} \leq 12.5 \text{ m/s ,} \\ [0.085(-0.56u_*^2 + 20.255u_*) + 2.458] - 0.58] \times 10^{-3} & \text{if } U_{10} > 12.5 \text{ m/s ,} \end{cases} \quad (3)$$

₁₆₀ with u_* the friction velocity. The relation between U_{10} and U_* is given by:

$$U_{10} = -0.56u_*^2 + 20.255u_* + 2.458 . \quad (4)$$

₁₆₁ The mesh resolution depends on the distance to the coastlines and reefs
₁₆₂ following the approach of Dobbelaere et al. (2020). The mesh is then further
₁₆₃ refined according to bathymetry value and gradient, as suggested in the
₁₆₄ SWAN user-guide³. Such an approach improves the model efficiency as the
₁₆₅ mesh resolution is only increased where required by the currents and waves
₁₆₆ dynamics. The mesh was generated with the seamsh⁴ Python library, which is
₁₆₇ based on the open-source mesh generator GMSH (Geuzaine and Remacle,
₁₆₈ 2009). It is composed of approximately 7.7×10^5 elements. The coarsest
₁₆₉ elements, far away from the FRT, have a characteristic length of about 5 km
₁₇₀ whereas the finest elements have a characteristic length of about 100 m along
₁₇₁ the coastlines and over the reefs (Fig 1).

₁₇₂ *2.4. Wave model*

₁₇₃ Waves were modeled using the parallel unstructured-mesh version of the
₁₇₄ Simulating WAves Nearshore (SWAN) model (Booij et al., 1999), one of the

³<http://swanmodel.sourceforge.net/unswan/unswan.htm>

⁴<https://pypi.org/project/seamsh/>

175 most popular wave models for coastal areas and inland waters. It solves the
176 action balance equation (Mei, 1989):

$$\frac{\partial N}{\partial t} + \nabla_{\mathbf{x}} \cdot [(\mathbf{c}_g + \mathbf{u})N] + \frac{\partial}{\partial \theta}[c_\theta N] + \frac{\partial}{\partial \sigma}[c_\sigma N] = \frac{S_{in} + S_{ds} + S_{nl}}{\sigma}, \quad (5)$$

177 where $N = E/\sigma$ is the wave action density and E is the wave energy spectrum;
178 θ is the wave propagation direction; σ is the intrinsic wave frequency; \mathbf{c}_g is
179 the wave group velocity, $\mathbf{u} = \mathbf{U}/H$ is SLIM depth-averaged current velocity;
180 c_θ and c_σ are the propagation velocities in spectral space due to refraction
181 and shifting in frequency due to variations in depth and currents; and S_{in} ,
182 S_{ds} , and S_{nl} respectively represent wave growth by wind, wave decay and
183 nonlinear transfers of wave energy through interactions between triplets and
184 quadruplets. The wave spectra were discretized with 48 direction bins and 50
185 frequency bins logarithmically distributed from 0.03 to 2 Hz. Exponential
186 wind growth was parameterized using the formulation of Janssen (1991), while
187 dissipations by whitecapping and bottom dissipation followed the formulations
188 of Komen et al. (1984) and Madsen et al. (1989), respectively.

189 Coefficients for exponential wind growth and whitecapping parameteriza-
190 tions were based on the results of Siadatmousavi et al. (2011), and significantly
191 differ from SWAN's default settings. By default, SWAN implements the wind
192 input formulation of Komen et al. (1984) and the steepness-dependent co-
193 efficient governing dissipation by whitecapping is a linear function of the
194 wavenumber. In this study, this steepness-dependent coefficient is a quadratic
195 function of the wavenumber, as it showed better predictions of the significant
196 wave height in the study of Siadatmousavi et al. (2011). The choice of these
197 formulations was motivated by the appearance of numerical instabilities in
198 the region of the Gulf Stream when using SWAN's default parameter values.
199 Finally, wave boundary conditions were derived from WAVEWATCH III
200 (Tolman et al., 2009) spectral outputs at NDBC buoy locations. We selected
201 these datasets as the large number of NDBC buoys around our region of
202 interest allowed for a fine representation of the wave spectra on the boundary

203 of the domain.

204 Surface waves induce a net drift in the direction of the wave propagation,
205 known as the Stokes drift (Van Den Bremer and Breivik, 2018; Stokes,
206 1880). This net drift has a significant impact on sediment transport in
207 nearshore regions (Hoefel and Elgar, 2003), on the formation of Langmuir
208 cells (Langmuir, 1938; Craik and Leibovich, 1976) as well as on the transport
209 of heat, salt or pollutants such as oil or micro-plastic in the upper ocean layer
210 (McWilliams and Sullivan, 2000; Röhrs et al., 2012; Drivdal et al., 2014). To
211 correctly model the Stokes drift profile in mixed wind-driven sea and swell
212 conditions, the full two-dimensional wave spectrum must be represented by a
213 spectral wave model within a wave-current coupling (Van Den Bremer and
214 Breivik, 2018). We therefore used SWAN modeled spectra to compute the
215 Stokes drift as follows:

$$\mathbf{u}_s = \int_0^{2\pi} \int_0^{+\infty} \frac{\sigma^3}{h \tanh(2kh)} E(\sigma, \theta) (\cos \theta, \sin \theta) d\sigma d\theta , \quad (6)$$

216 where k is the norm of the wave vector; h is the water depth; and $E(\sigma, \theta)$ is
217 the wave energy density.

218 2.5. Coupled model

219 SLIM and SWAN are coupled so that they run on the same computational
220 core and the same unstructured mesh. SLIM is run first and passes the
221 wind velocity (\mathbf{U}_{10}), water level ($\eta = H - h$) and depth-averaged current
222 ($\mathbf{u} = \mathbf{U}/H$) fields to SWAN, as well as a roughness length (z_0) for the bottom
223 dissipation formulation of Madsen et al. (1989). This roughness length is
224 computed from SLIM's bulk drag coefficient C_b following the approach of
225 Dietrich et al. (2011) so that both models have consistent bottom dissipation
226 parameterizations. SWAN then uses these quantities to compute the wave
227 radiation stress gradient, that is then passed to SLIM as the force exerted
228 by waves on currents $\boldsymbol{\tau}_{\text{wave}}$ (Fig. 3). SLIM then uses this quantity to
229 update the value of the surface stress $\boldsymbol{\tau}_s$ in Eq. (1), that now becomes

the sum of wind and wave-induced stresses $\tau_s = \tau_{\text{wind}} + \tau_{\text{wave}}$. Here, the momentum flux from the atmosphere to the ocean is taken as the commonly used full wind stress τ_{wind} . Doing so, we neglect the momentum advected away from the storm by the waves, leading to a 10-15% overestimation of the momentum flux in hurricane winds (Curcic, 2015). Moreover, we followed the approach of Dietrich et al. (2012) by characterizing the wave-induced stresses using the radiation-stress representation instead of the vortex-force representation (McWilliams et al., 2004). Although the latter provides a clearer and more meaningful decomposition of the wave effect, we implemented the first representation for the sake of simplicity as it allows us to provide the whole wave contribution as an additional surface stress to SLIM (Lane et al., 2007).

SLIM's governing equations are integrated using an implicit time integration scheme while SWAN is unconditionally stable (Dietrich et al., 2012), allowing both models to be run with relatively large time steps. In this study, the stationary version of SWAN was used, *i.e.* the time derivative of Eq. (5) was set to zero. This resulted in reduced scaling and convergence rates than with the nonstationary version of SWAN but increased the stability of the model. The wave spectra at each node of the mesh was saved at the end of each iteration to serve as initial conditions for the next one. Both models were run sequentially using a time step of 600 s, so that each computational core was alternatively running either SLIM or SWAN. As in the coupling between SWAN and ADCIRC (Dietrich et al., 2012), both models use the same local sub-mesh, allowing for a one-to-one correspondence between the geographic locations of the mesh vertices. No interpolation is therefore needed when passing the discretised variables from one model to the other, which allows an efficient inter-model communication. However, as SLIM is based on a discontinuous Galerkin finite element method, an additional conversion step to a continuous framework was required to transfer SLIM nodal quantities to SWAN.

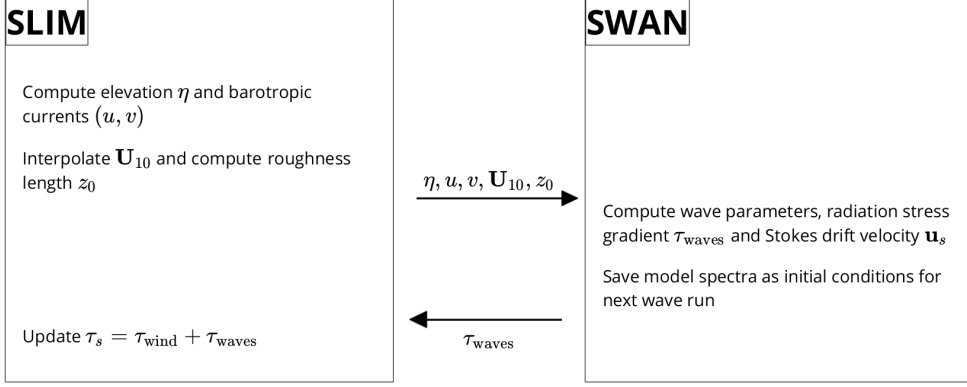


Fig. 3: Schematic illustration of the coupled SLIM+SWAN model.

260 *2.6. Quantifying the effect of wave-current interactions on transport*

261 To quantify the impact of wave-current interactions on transport processes,
 262 we compared the trajectories of passive particles advected by the uncoupled
 263 SLIM and coupled SLIM+SWAN currents during the passage of Irma in the
 264 Lower Keys. Furthermore, the depth-averaged Stokes drift was computed
 265 using the wave spectra of the coupled model SLIM+SWAN run as well as
 266 those of an uncoupled SWAN run. Particles were released on the inner and
 267 outer shelves at the points highlighted by red and blue dots in Fig. 4 on
 268 Sept. 7 at 0000 UTC and then tracked until Sept. 15. These initial particle
 269 positions were found using backtracking methods (Spivakovskaya et al., 2005)
 270 to ensure that the release particles would intersect the path of Irma during
 271 its passage through the Florida Keys. We first defined two 25 km² circular
 272 regions on the trajectory of the hurricane (see red and blue circles in Fig. 4).
 273 Particles within these two regions were then tracked backward in time using
 274 uncoupled SLIM currents from the exact time of the passage of the hurricane
 275 until Sept. 7 at 0000 UTC. Their positions at the end of the backward
 276 simulation (see red and blue particle clouds in Fig. 4) corresponds to the
 277 initial condition of the forward transport simulations described below. We
 278 then compared the trajectories of particles originating from these regions and

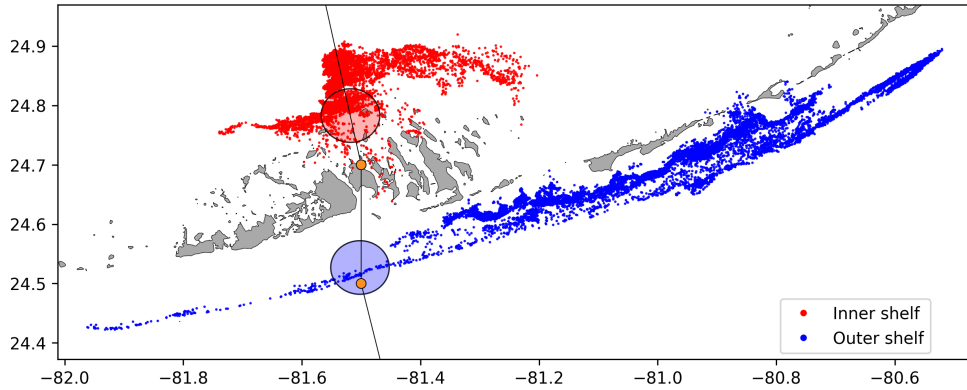


Fig. 4: Release regions of the passive particles on the inner and outer shelves (red and blue clouds) obtained by backtracking particles released in the red and blue circular areas during the passage of Irma.

advedted forward in time by different sets of currents: (i) uncoupled SLIM currents alone; (ii) coupled SLIM+SWAN currents; (iii) SLIM currents with the addition of the depth-averaged Stokes drift computed with the coupled wave-current model (Stokes-C); (iv) SLIM+SWAN currents with Stokes-C; and (v) SLIM currents with the depth-averaged Stokes drift computed with the uncoupled wave model (Stokes-U). Particle trajectories are compared by computing the distances between the centers of mass of the particle clouds through time.

3. Results

We first validated the reconstructed atmospheric fields of hurricane Irma as well as the outputs of our coupled wave-current model against field measurements. We then used the validated model outputs to simulate the transport of passive drifters in the Lower Keys during the passage of Hurricane Irma. These drifters were advected by the sets of currents described in section 2.6 and their trajectories were compared to evaluate the impact of the wave-current interactions and the Stokes drift on the transport processes during the passage of Irma.

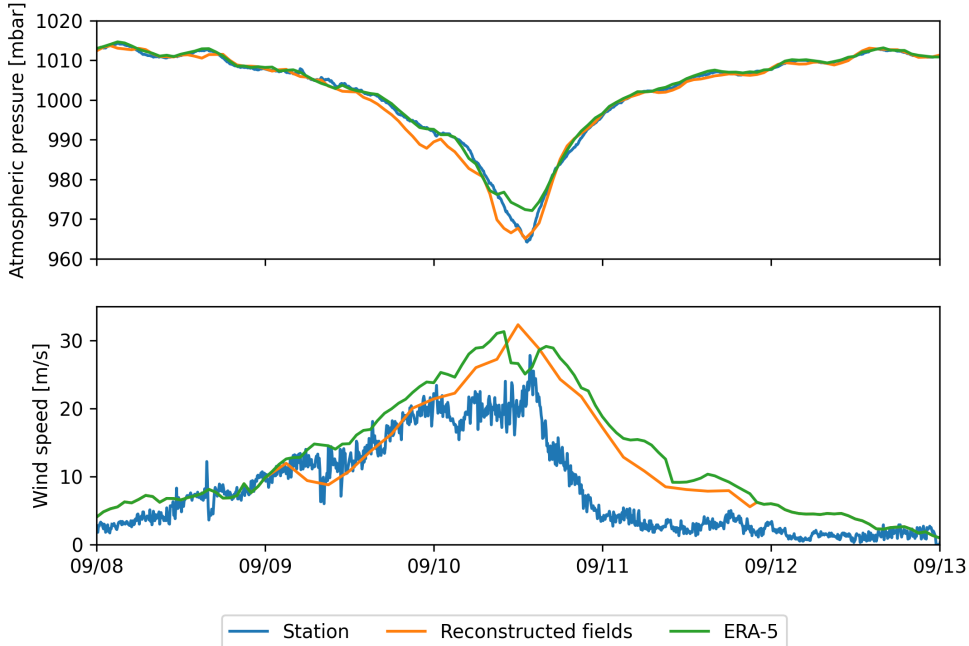


Fig. 5: Comparison of reconstructed wind atmospheric pressure with field measurements and coarser ECMWF ERA-5 profiles at Vaca Key station. The generated hybrid atmospheric forcings better reproduce the observed storm depression while H*wind winds better reproduce the measured peak in wind speed.

296 3.1. *Model validation*

297 H*Wind winds and hybrid pressure field agree well with station mea-
 298 surements at Vaca Key station (Fig. 5). The hybrid pressure field shows a
 299 better agreement with observations than ERA-5 pressure as it successfully
 300 reproduces the storm depression. ERA-5 fields, on the other hand, fail to
 301 reproduce the low pressure at the core of the hurricane due to their coarser
 302 grid, leading to an overestimation of 8 mbar of the storm depression. Both
 303 H*Wind and ERA-5 agree well with observed wind speeds although both
 304 data sets tend to slightly overestimate the width and intensity of the wind
 305 peak. However, H*wind profiles better reproduce the timing of the observed
 306 peak, as ERA-5 winds tend to anticipate it. H*wind also exhibits a slightly
 307 narrower peak in wind speed, which better agrees with observations.

308 Hydrodynamic outputs of the coupled wave-current model agree well with
309 tide gauge (Fig. 6) and ADCP measurements (Fig. 7). Despite a slight
310 overestimation of the amplitude of sea surface elevation (Table 1) in fair
311 weather conditions, the timing and amplitude of the storm surges are well
312 reproduced by the coupled model. The largest model error during the surge
313 is an overestimation of 18 cm of the elevation peak at Virginia Key. The fit is
314 especially good at Naples, where both the large positive and negative surges
315 are captured by the coupled model with an error of less than 5 cm. modeled
316 2D currents were validated against depth-averaged ADCP measurements
317 at mooring stations C10, C12 and C13 (Fig. 7). As in Liu et al. (2020),
318 we performed the vector correlation analysis of Kundu (1976) to compare
319 modeled and observed current velocity vectors. Correlation coefficients (ρ)
320 between simulated and observed depth-averaged currents are 0.84, 0.74 and
321 0.73 at stations C10, C12 and C13, respectively. The average veering angles
322 are below 12°, as in (Liu et al., 2020). Furthermore, the positive bias in Table
323 1 indicates that our model tends to underestimate the southward component
324 of the currents at the different stations. As expected from a depth-averaged
325 model, the best fit with observations is obtained at the shallowest mooring
326 C10, located on the 25 m isobath, with an average veering angle of 6° and
327 smaller error statistics (Table 1).

328 The simulated significant wave height agrees well with observations on
329 the WFS, where errors on the peak value do not exceed 5% (Fig. 8). On
330 Florida's eastern shelf, errors are slightly larger and reach 20%. Although the
331 model outputs agree well with observations, a lag in significant wave height is
332 observed for all 4 buoys. Moreover, the peak in significant wave height tends
333 to be underestimated at buoys 41113 and 41114, located on the eastern shelf
334 of Florida. The same tendency is observed with the modeled wave period,
335 with mean errors inferior to 1 second on the WFS and reaching more than
336 2 seconds on Florida's eastern shelf (Table 1), as the coupled model fails
337 to reproduce the observed peak in wave period between the 7th and 8th of

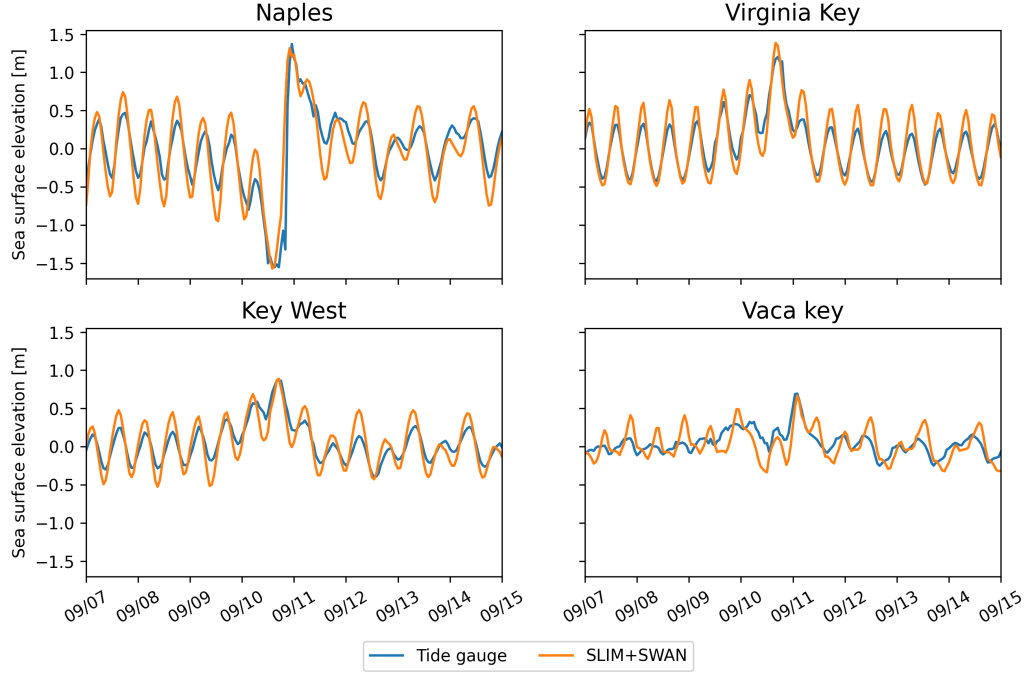


Fig. 6: Comparison of modeled sea surface elevation at the 4 tide gauges shown in Fig. 1B. The timing and amplitudes of the storm surges are well reproduced by the model

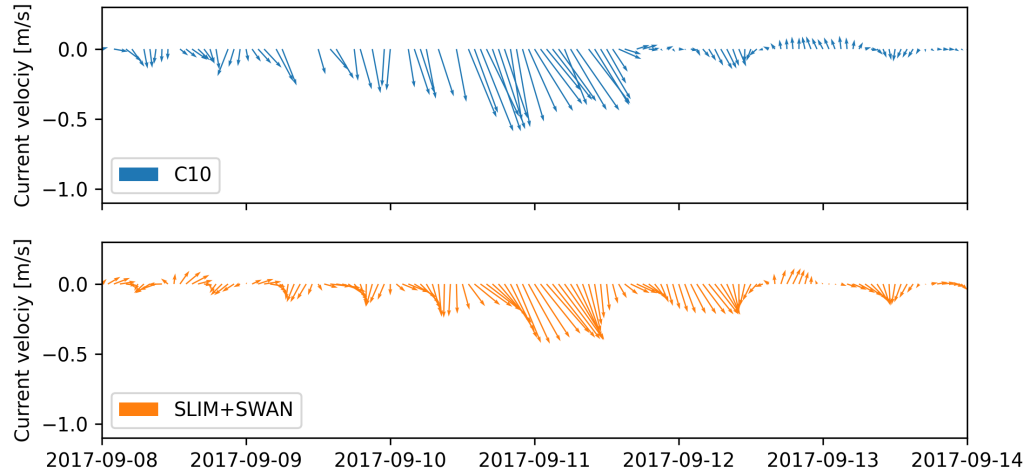


Fig. 7: Comparison of modeled current velocity with observed velocity at mooring C10 (see Fig. 1B for its location). modeled current velocities agree well with observations, with a correlation coefficient of 0.83 and an average veering angle of 6°.

338 September on this side of Florida. Finally, modeled wave direction agrees well
339 with observation (Fig. 8), although our model tends to overestimate wave
340 propagation in the northward direction at stations 41114 and 41113 on the
341 passage of the hurricane.

342 *3.2. Impact of waves on currents and transport*

343 We evaluated the impact of wave-current interactions on modeled currents
344 during the passage of Irma in the Lower Keys, between Sept. 7 and 13, 2017.
345 First, we computed the maximum difference between currents modeled by
346 SLIM and SLIM+SWAN during this period (Fig. 9A). The largest differences
347 in current speed were observed over the reefs, on the shelf break and around
348 islands. They locally reach 1 m/s, with the coupled SLIM+SWAN model
349 yielding the largest amplitudes. The regions where the differences are the
350 largest experience the strongest radiation-stress gradient τ_{wave} (Fig. 9B)
351 induced by wave energy dissipation on the shelf-break and rough seabed
352 induce variations of the wave radiation stress (Longuet-Higgins and Stewart,
353 1964). This highlights the important protective role of the barrier formed
354 by the offshore reefs, that require a fine spatial resolution to be accurately
355 captured. Wave-induced differences in current speed were amplified by the
356 action of the wind stress τ_{wind} (Fig. 9C). Wind speeds were larger in the front
357 right quadrant of the hurricane (Zedler et al., 2009), yielding larger differences
358 on the right-hand side of the storm trajectory. This is especially clear in the
359 area between the Florida Keys and the Everglades, where relatively small
360 values of τ_{wave} nonetheless produce current speed differences of up to 0.5 m/s
361 because of the wind stress.

362 Waves play a significant role on the transport processes during and after the
363 passage of hurricane Irma (Fig. 10A,B). Comparing SLIM and SLIM+SWAN
364 shows that wave-current interactions alone yield differences of up to 5 km
365 between the modeled trajectories on the passage of the hurricane. These
366 differences exceed 10 km on the outer shelf when Stokes drift is taken into
367 account. The impact of the waves on the transport processes differs signifi-

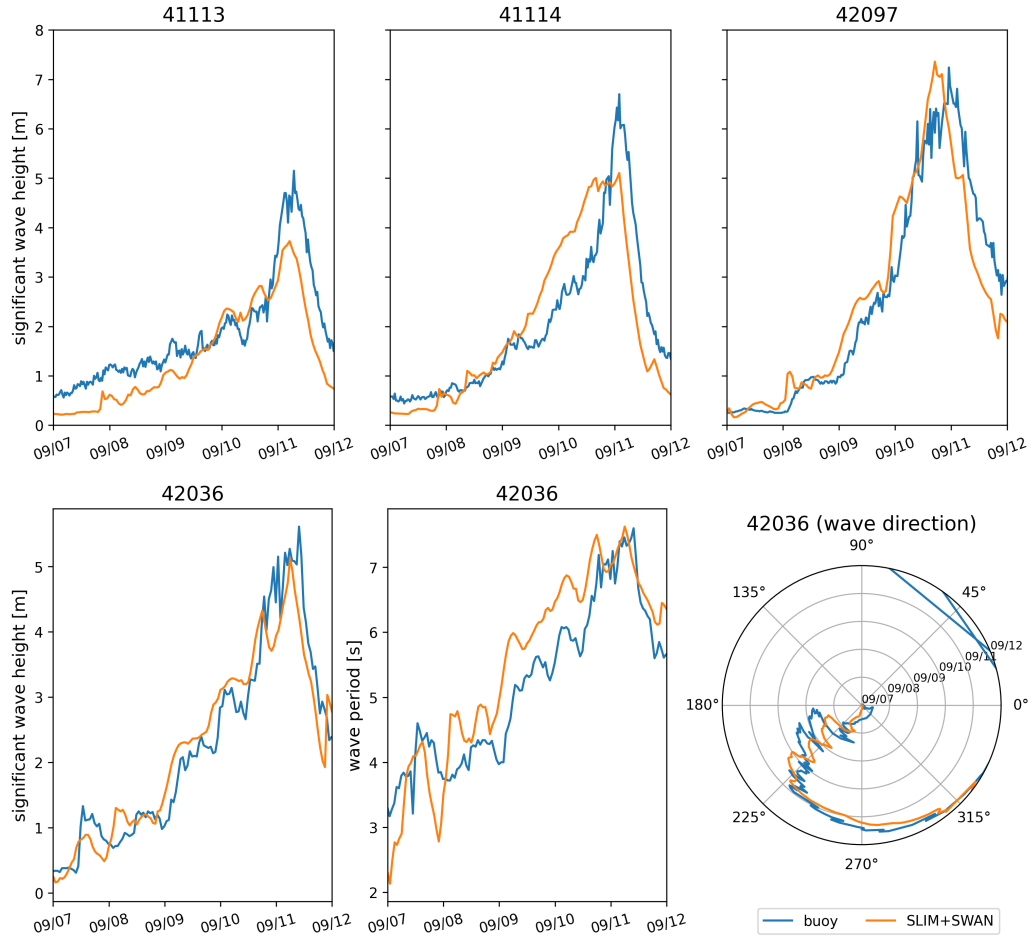


Fig. 8: Comparison of modeled wave parameters with observation at the 4 buoys location (locations shown in Fig. 1B). The modeled significant wave heights agree well with field measurement.

Station	Variable	Bias	MAE	RMSE
Vaca Key	sse (m)	n/a	0.12	0.16
	U_{10} (m/s)	1.51	1.85	2.61
	p_{atm} (hPa)	-0.21	0.59	1.03
Key West	sse (m)	n/a	0.11	0.13
Virginia Key	sse (m)	n/a	0.10	0.13
Naples	sse (m)	n/a	0.18	0.23
C10	u (m/s)	-0.006	0.04	0.05
	v (m/s)	0.02	0.06	0.08
C12	u (m/s)	-0.01	0.06	0.07
	v (m/s)	0.06	0.09	0.11
C13	u (m/s)	0.004	0.06	0.08
	v (m/s)	0.04	0.06	0.08
41113	H_s (m)	-0.35	0.40	0.51
	T_m (s)	-2.18	2.47	3.13
	θ_m (degree)	7.17	19.50	26.06
41114	H_s (m)	-0.21	0.53	0.68
	T_m (s)	-1.69	2.53	3.15
	θ_m (degree)	31.25	35.28	46.18
42036	H_s (m)	-0.03	0.26	0.36
	T_m (s)	0.04	0.65	0.77
	θ_m (degree)	19.92	30.65	41.69
42097	H_s (m)	-0.15	0.40	0.57
	T_m (s)	0.02	0.62	0.74
	θ_m (degree)	3.62	28.08	45.89

Table 1: Error statistics on the wave-current model outputs as compared to the measured sea surface elevation (sse), eastward and northward depth-average current velocities (u,v), significant wave height (H_s), zero-crossing mean wave period (T_m) and mean wave direction (θ_m). Model bias, mean absolute error (MAE), and root mean squared error (RMSE) are listed by variable (unit) and value.

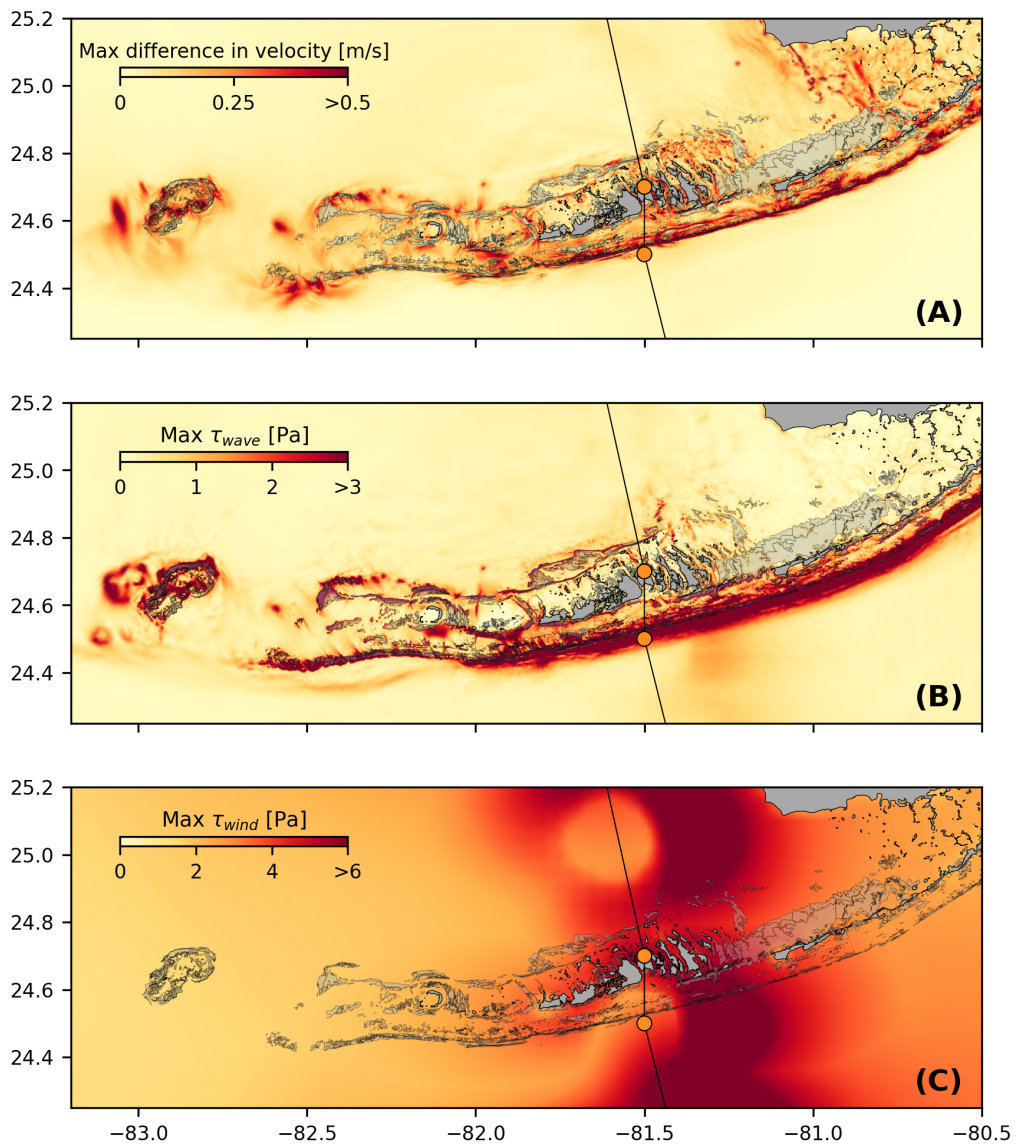


Fig. 9: (A). Maximum difference between SLIM and SLIM+SWAN currents during the passage of Irma in the Lower Florida Keys; (B) Maximum wave radiation stress gradient τ_{wave} and (C) maximum wind stress τ_{wind} (C) generated by the hurricane. Radiation stress gradient yields difference larger than 0.5 m/s (and locally reaching 1m/s) in current velocities, especially over offshore reefs.

368 cantly between the inner and outer shelves, with wave-induced differences in
369 trajectories 4 to 5 times larger on the outer shelf. Furthermore, the distance
370 between the centers of mass of the clouds of particles tends to stabilize on
371 the inner shelf after the passage of Irma, while it keeps increasing on the
372 other shelf up to two days after the passage of the hurricane when taking
373 Stokes drift into account. The distance then stabilizes for about a day before
374 it starts decreasing (see right panel of Fig. 10A,B). However, when consider-
375 ing wave-current interactions alone (SLIM vs. SLIM+SWAN), the distance
376 between the clouds of particles starts to decrease just after the passage of
377 Irma.

378 The Stokes drift appears to have a larger effect than the radiation stress
379 gradient and the wave-current interactions (Fig 10A,B). Nonetheless, compar-
380 ing the different curves for the outer shelf suggests that the radiation-stress
381 gradient induces effects similar to the impact of the Stokes drift in this
382 region during the passage of Irma. However, when comparing SLIM and
383 SLIM+SWAN both on the inner and other shelf, this impact appears to be
384 negligible during the rest of the simulation. Comparing Stokes-U and Stokes-C
385 indicates that the difference between the trajectories of particles advected by
386 the two Stokes drifts does not exceed 2 km, with larger discrepancies on the
387 outer shelf (Fig. 10C,D). The distance between the two clouds of particles
388 increases abruptly on the passage of the hurricane (and two days after on the
389 outer shelf) and then stabilizes during the rest of the simulation.

390 4. Discussion

391 The coupled SLIM+SWAN model correctly reproduces the hydrodynamics
392 and wave dynamics during hurricane Irma. Such good agreement with field
393 measurements can only be achieved using accurate forcings and adequate
394 wave parameterizations. By comparing coupled and uncoupled model runs, we
395 showed that neglecting wave radiation stress gradient can induce differences
396 of up to 1 m/s in modeled current velocities. The radiation stress gradient

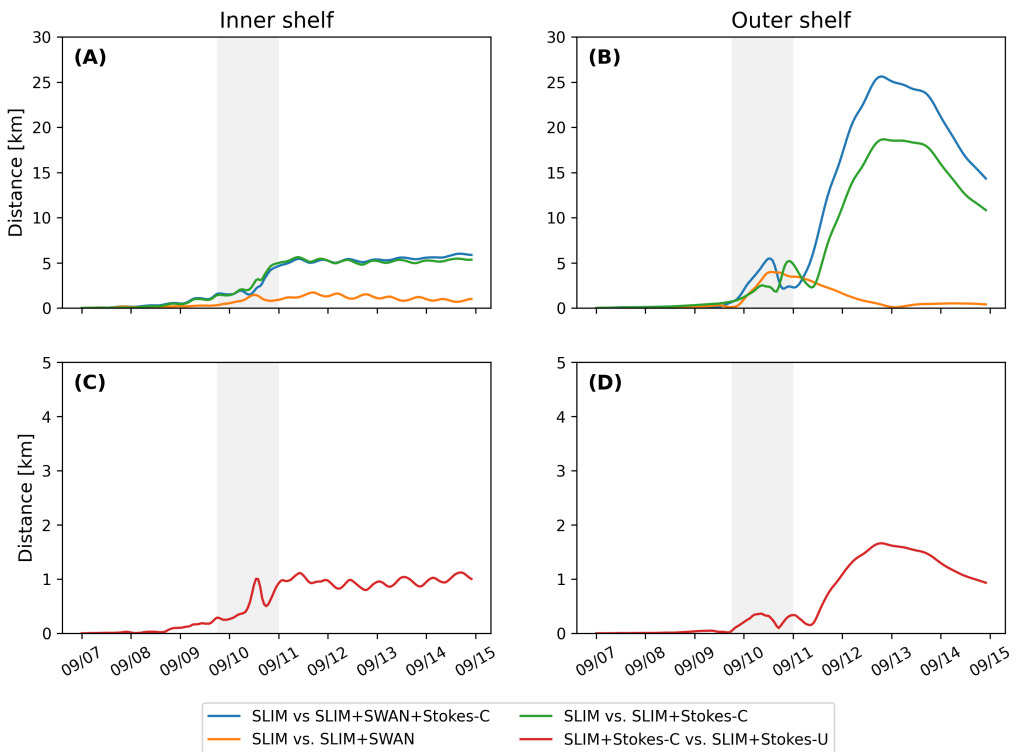


Fig. 10: Difference between the centers of mass of the particle clouds released from the regions highlighted in Fig. 4 and advected by different combinations of coupled and uncoupled velocity fields.

397 during the hurricane was especially large over the shelf break, where waves
398 are strongly dissipated by the offshore coral reef barrier. The radiation stress
399 gradient alone can deflect drifting particles by up to 5 km during the passage
400 of the hurricane. These differences in modeled trajectories were significantly
401 larger and required more time to stabilize on the outer shelf. The impact of
402 the Stokes drift dominates the effects of wave-current interactions through the
403 radiation stress gradient, except during the passage of the hurricane, when
404 both contributions are similar. Finally, neglecting wave-current interactions
405 when computing Stokes drift leads to variations of up to 2 km in modeled
406 trajectories on the passage of the hurricane.

407 Despite slightly overestimating the amplitude of the sea surface elevation in
408 fair weather conditions, the coupled wave-current model correctly reproduces
409 the timing and amplitude of the observed storm surge. All elevation peaks are
410 captured with a 4% accuracy at every station except Virginia key, where the
411 surge was overestimated by about 15%. Such accuracy is key to predict the
412 damages caused by the hurricane, as most destroyed and severely damaged
413 buildings in the Florida Keys during Hurricane Irma were caused by storm
414 surge and waves (Xian et al., 2018). Furthermore, by using a high-resolution
415 model, we can explicitly reproduce the circulation between all the reefs and
416 islands of the Florida Keys. The fine-scale details of the storm surge, and
417 hence the associated risk, are thus accurately represented. In addition to
418 accurately capturing positive surges, the model also reproduced the observed
419 negative surge in Naples with an error of about 1%. This result is of interest
420 from a biological point of view as negative surges, although less studied, affect
421 water exchanges between the estuaries and the coastal ocean and disturb
422 the benthic ecosystems (Liu et al., 2020). Such rapid decrease in water
423 level followed by a positive surge cause massive freshwater inflows, causing a
424 significant decrease in water salinity (Wachnicka et al., 2019).

425 Strong currents such as the Gulf Stream affect waves trough refraction
426 over gradients in current velocity, shoaling and breaking of opposing waves or

lengthening of following waves (Hegermiller et al., 2019). Under hurricane conditions, these interactions can cause numerical instabilities in the wave model if the parameterizations are not appropriate and the model resolution not sufficient. Hegermiller et al. (2019), for instance, used a 5-km model grid and 48 directional bins to capture spatial gradients in wave height induced by wave-currents interactions in the Gulf Stream during Hurricane Matthew (2016). We followed these guidelines when defining the coarsest resolution of the model mesh as well as the spectral discretization of SWAN. Boundary conditions and directional spreading of the incident waves also play a significant role when modeling wave-current interactions at meso- and submesoscales (Villas Bôas et al., 2020), which motivated our choice of imposing full spectra on the boundary of the wave model instead of bulk parameters. Finally, SWAN default parameterizations for wind energy input and whitecapping caused numerical instabilities by overestimating wave growth and steepness on the boundary of the Gulf Stream on the passage of Irma. This overestimation was solved by using the parameterization of Siadatmousavi et al. (2011). The parameters used in this study were calibrated on the Northern Gulf of Mexico, which might explain that our model better reproduces wave parameters at buoys located on the WFS. However, these calibrated parameters might underestimate wind-induced wave growth on Florida's eastern shelf. Consequently, incident wave do not receive enough energy to grow after breaking on the bank boundary, leading to an underestimation of the significant wave height at buoys located on Florida's eastern shelf. A more extensive calibration study might therefore be necessary to further improve the agreement with field measurements on both sides of Florida. Nonetheless, as this study focuses on the wave produced by Irma, which made landfall on the West coast of Florida, the use of parameterizations calibrated for the Gulf of Mexico seems reasonable.

The radiation stress gradient significantly impacts currents during the passage of the hurricane. It can induce differences of up to 1 m/s in the

457 current speed on the shelf break. In this region waves are strongly dissipated
458 due to action of depth-induced breaking and bottom dissipation on coral reefs.
459 This highlights the protective role of coral reefs against strong incoming waves
460 (Lowe et al., 2005), which requires a sufficiently fine spatial resolution to be
461 explicitly represented in the model. Due to the dissipation of incoming waves
462 on the reefs, wave impact during Irma is different on the inner and outer
463 shelves. It is less important on the inner shelf because of the sheltering of the
464 inner shelf due to reefs and islands as well as wave breaking on the shelf break.
465 The inner shelf hence experiences weaker waves and currents, inducing weaker
466 and more localized transport. Furthermore, the impact of winds on waves
467 is reduced in shallower areas under the action of depth-induced breaking.
468 This might explain why differences between particle trajectories stabilize
469 on the inner shelf just after the passage of Hurricane Irma. However, the
470 Florida Keys still experienced strong winds after the passage of the core of the
471 hurricane, which generated high waves in the deeper areas. This might explain
472 why the differences on between the modeled trajectories kept increasing on
473 the outer shelf under the action of strong Stokes drift up to two days after
474 the passage of the hurricane.

475 The distance between the centers of mass of the particle clouds advected
476 by coupled and uncoupled Stokes drift remains rather limited (< 2 km). This
477 suggest that taking wave-current interactions into account when computing
478 Stokes drift, even in heavy wind conditions has a limited impact. Furthermore,
479 combining the coupled Stokes drift with the coupled and uncoupled SLIM
480 currents produced similar trajectories on the inner shelf, which seems to
481 indicate that wave impact on currents is limited in this region. This would
482 suggest that it is not necessary to take wave-current interactions into account
483 when modeling the trajectories of tracers in shallow, sheltered areas such
484 as the inner WFS during a hurricane. Uncoupled currents with uncoupled
485 Stokes drift should give a reasonably accurate approximation of the transport
486 processes. However, this does not hold for deeper and unsheltered regions,

487 as highlighted by the comparison of trajectories obtained with coupled and
488 uncoupled SLIM currents combined with coupled Stokes drift on the outer
489 shelf.

490 **5. Conclusion**

491 We developed a coupled wave-current model to study the impact of waves
492 on transport processes during Hurricane Irma. In order to accurately represent
493 the wind and pressure profiles of the hurricane, we built hybrid fields by
494 combining coarser ERA-5 data with high-resolution H*Wind data for the wind
495 speed and idealized Holland profiles for the pressure. Comparing these hybrid
496 profiles with field observations showed that they were better at reproducing the
497 observed central depression of the hurricane as well as the peak in wind speed
498 than ERA-5 data. Using these hybrid fields as forcings, our coupled model
499 accurately reproduced the storm surge at tide gauge locations and produced
500 currents and wave parameters in good agreement with field observations,
501 especially on the WFS. The modeled currents and Stokes drift were then used
502 to evaluate the impact of waves on the trajectory of passive drifters on the
503 passage of the hurricane through the Florida Keys. Our results show that
504 waves had a significant impact on heavy-wind transport processes and caused
505 deflections of the drifters trajectories by more than 20 km on the outer shelf.

506 Despite its good agreement with observations, our model could be fur-
507 ther refined by improving the representation of wind-wave interactions. In
508 particular, it does not consider the momentum loss due to the action of
509 surface waves when representing momentum flux from the atmosphere to the
510 ocean, leading to overestimations under hurricane conditions. Our model
511 could therefore be further improved by using wave-dissipative stress instead
512 of the full wind stress as the momentum flux from the atmosphere to the
513 ocean. Moreover, a more thorough calibration of the wave model parameters
514 should improve our model results on Florida's eastern shelf. Finally, as a 2D
515 barotropic model, SLIM does not explicitly represent baroclinic phenomenons

516 as well as the vertical profile of the Stokes drift and radiation stress gradient
517 along the wave boundary layer. However, our study focused on relatively
518 shallow and vertically homogeneous coastal waters using a reef-scale resolution
519 throughout the whole FRT. Such fine resolution allows to explicitly represent
520 wave dissipation over coral reefs and is only achievable using a 2D model due
521 to computational resources limitations.

522 Wave coupling needs to be taken into account during heavy-wind events
523 but not necessarily in milder conditions. While the radiation stress gradient
524 plays an important role and can lead to differences of up to 5 km, the
525 Stokes drift is about 4 times more intense and should thus be considered
526 in priority. This study brings new insight on the impact of waves on the
527 transport processes nearshore during a tropical cyclone. Due to its high
528 spatial resolution, the developed coupled wave-current model can be used
529 to accurately represent the dispersal of pollutants, sediments or larvae in
530 topologically complex coastal areas in heavy-wind conditions.

531 Acknowledgments

532 Computational resources were provided by the Consortium des Équipements
533 de Calcul Intensif (CÉCI), funded by the F.R.S.-FNRS under Grant No.
534 2.5020.11. Thomas Dobbelaere is a PhD student supported by the Fund for
535 Research training in Industry and Agriculture (FRIA/FNRS).

536 References

- 537 Bever, A.J., MacWilliams, M.L., 2013. Simulating sediment transport pro-
538 cesses in San Pablo Bay using coupled hydrodynamic, wave, and sediment
539 transport models. *Marine Geology* 345, 235–253.
- 540 Bhatia, K.T., Vecchi, G.A., Knutson, T.R., Murakami, H., Kossin, J., Dixon,
541 K.W., Whitlock, C.E., 2019. Recent increases in tropical cyclone intensifi-
542 cation rates. *Nature Communications* 10, 1–9.

- 543 Booij, N., Ris, R.C., Holthuijsen, L.H., 1999. A third-generation wave
544 model for coastal regions: 1. Model description and validation. *Journal of*
545 *Geophysical Research: Oceans* 104, 7649–7666.
- 546 Breivik, Ø., Allen, A.A., Maisondieu, C., Olagnon, M., 2013. Advances in
547 search and rescue at sea. *Ocean Dynamics* 63, 83–88.
- 548 Chassignet, E.P., Hurlburt, H.E., Smedstad, O.M., Halliwell, G.R., Hogan,
549 P.J., Wallcraft, A.J., Baraille, R., Bleck, R., 2007. The HYCOM (hybrid
550 coordinate ocean model) data assimilative system. *Journal of Marine*
551 *Systems* 65, 60–83.
- 552 Craik, A.D., Leibovich, S., 1976. A rational model for Langmuir circulations.
553 *Journal of Fluid Mechanics* 73, 401–426.
- 554 Curcic, M., 2015. Explicit air-sea momentum exchange in coupled atmosphere-
555 wave-ocean modeling of tropical cyclones. Ph.D. thesis. University of Miami.
- 556 Curcic, M., Chen, S.S., Özgökmen, T.M., 2016. Hurricane-induced ocean
557 waves and stokes drift and their impacts on surface transport and dispersion
558 in the Gulf of Mexico. *Geophysical Research Letters* 43, 2773–2781.
- 559 Curcic, M., Haus, B.K., 2020. Revised estimates of ocean surface drag in
560 strong winds. *Geophysical Research Letters* 47, e2020GL087647.
- 561 Dietrich, J., Bunya, S., Westerink, J., Ebersole, B., Smith, J., Atkinson,
562 J., Jensen, R., Resio, D., Luettich, R., Dawson, C., et al., 2010. A high-
563 resolution coupled riverine flow, tide, wind, wind wave, and storm surge
564 model for southern Louisiana and Mississippi. Part II: Synoptic description
565 and analysis of Hurricanes Katrina and Rita. *Monthly Weather Review*
566 138, 378–404.
- 567 Dietrich, J., Westerink, J., Kennedy, A., Smith, J., Jensen, R., Zijlema, M.,
568 Holthuijsen, L., Dawson, C., Luettich, R., Powell, M., et al., 2011. Hurricane

- 569 Gustav (2008) waves and storm surge: Hindcast, synoptic analysis, and
570 validation in southern Louisiana. *Monthly Weather Review* 139, 2488–2522.
- 571 Dietrich, J.C., Tanaka, S., Westerink, J.J., Dawson, C., Luettich, R., Zijlema,
572 M., Holthuijsen, L.H., Smith, J., Westerink, L., Westerink, H., 2012. Per-
573 formance of the unstructured-mesh, SWAN+ ADCIRC model in computing
574 hurricane waves and surge. *Journal of Scientific Computing* 52, 468–497.
- 575 Dobbelaere, T., Muller, E.M., Gramer, L.J., Holstein, D.M., Hanert, E., 2020.
576 Coupled epidemi-hydrodynamic modeling to understand the spread of a
577 deadly coral disease in Florida. *Frontiers in Marine Science* 7, 1016.
- 578 Donelan, M., Haus, B., Reul, N., Plant, W., Stiassnie, M., Gruber, H., Brown,
579 O., Saltzman, E., 2004. On the limiting aerodynamic roughness of the
580 ocean in very strong winds. *Geophysical Research Letters* 31.
- 581 Drivdal, M., Broström, G., Christensen, K., 2014. Wave-induced mixing and
582 transport of buoyant particles: Application to the Statfjord A oil spill.
583 *Ocean Science* 10, 977–991.
- 584 Figueiredo, J., Baird, A.H., Connolly, S.R., 2013. Synthesizing larval com-
585 petence dynamics and reef-scale retention reveals a high potential for
586 self-recruitment in corals. *Ecology* 94, 650–659.
- 587 Fringer, O.B., Dawson, C.N., He, R., Ralston, D.K., Zhang, Y.J., 2019. The
588 future of coastal and estuarine modeling: Findings from a workshop. *Ocean*
589 *Modelling* 143, 101458.
- 590 Frys, C., Saint-Amand, A., Le Hénaff, M., Figueiredo, J., Kuba, A., Walker,
591 B., Lambrechts, J., Vallaeyns, V., Vincent, D., Hanert, E., 2020. Fine-scale
592 coral connectivity pathways in the Florida Reef Tract: Implications for
593 conservation and restoration. *Frontiers in Marine Science* 7, 312.

- 594 Geuzaine, C., Remacle, J.F., 2009. Gmsh: A 3-d finite element mesh generator
595 with built-in pre-and post-processing facilities. International journal for
596 numerical methods in engineering 79, 1309–1331.
- 597 Harper, B., Kepert, J., Ginger, J., 2010. Guidelines for converting between
598 various wind averaging periods in tropical cyclone conditions.
- 599 Hegermiller, C.A., Warner, J.C., Olabarrieta, M., Sherwood, C.R., 2019.
600 Wave-current interaction between Hurricane Matthew wave fields and the
601 Gulf Stream. Journal of Physical Oceanography 49, 2883–2900.
- 602 Hoefel, F., Elgar, S., 2003. Wave-induced sediment transport and sandbar
603 migration. Science 299, 1885–1887.
- 604 Holthuijsen, L.H., Powell, M.D., Pietrzak, J.D., 2012. Wind and waves in
605 extreme hurricanes. Journal of Geophysical Research: Oceans 117.
- 606 Janssen, P.A., 1991. Quasi-linear theory of wind-wave generation applied to
607 wave forecasting. Journal of Physical Oceanography 21, 1631–1642.
- 608 Johns, W.E., Schott, F., 1987. Meandering and transport variations of the
609 Florida Current. Journal of Physical Oceanography 17, 1128–1147.
- 610 Knaff, J.A., Sampson, C.R., Musgrave, K.D., 2018. Statistical tropical cyclone
611 wind radii prediction using climatology and persistence: Updates for the
612 western North Pacific. Weather and Forecasting 33, 1093–1098.
- 613 Knutson, T., Camargo, S.J., Chan, J.C., Emanuel, K., Ho, C.H., Kossin, J.,
614 Mohapatra, M., Satoh, M., Sugi, M., Walsh, K., et al., 2020. Tropical
615 cyclones and climate change assessment: Part II: Projected response to
616 anthropogenic warming. Bulletin of the American Meteorological Society
617 101, E303–E322.

- 618 Komen, G., Hasselmann, S., Hasselmann, K., 1984. On the existence of a
619 fully developed wind-sea spectrum. *Journal of Physical Oceanography* 14,
620 1271–1285.
- 621 Kossin, J.P., Knapp, K.R., Olander, T.L., Velden, C.S., 2020. Global increase
622 in major tropical cyclone exceedance probability over the past four decades.
623 *Proceedings of the National Academy of Sciences* 117, 11975–11980.
- 624 Kourafalou, V.H., Kang, H., 2012. Florida Current meandering and evo-
625 lution of cyclonic eddies along the Florida Keys Reef Tract: Are they
626 interconnected? *Journal of Geophysical Research: Oceans* 117.
- 627 Kundu, P.K., 1976. Ekman veering observed near the ocean bottom. *Journal*
628 *of Physical Oceanography* 6, 238–242.
- 629 Lambrechts, J., Hanert, E., Deleersnijder, E., Bernard, P.E., Legat, V.,
630 Remacle, J.F., Wolanski, E., 2008. A multi-scale model of the hydrodynam-
631 ics of the whole Great Barrier Reef. *Estuarine, Coastal and Shelf Science*
632 79, 143–151.
- 633 Landsea, C.W., Franklin, J.L., 2013. Atlantic hurricane database uncertainty
634 and presentation of a new database format. *Monthly Weather Review* 141,
635 3576–3592.
- 636 Lane, E.M., Restrepo, J., McWilliams, J.C., 2007. Wave-current interaction:
637 A comparison of radiation-stress and vortex-force representations. *Journal*
638 *of Physical Oceanography* 37, 1122–1141.
- 639 Langmuir, I., 1938. Surface motion of water induced by wind. *Science* 87,
640 119–123.
- 641 Le, H.A., Lambrechts, J., Ortaleb, S., Gratiot, N., Deleersnijder, E., Soares-
642 Frazão, S., 2020. An implicit wetting–drying algorithm for the discontinuous
643 galerkin method: application to the tonle sap, mekong river basin. *Envi-
644 ronmental Fluid Mechanics* , 1–29.

- 645 Le Hénaff, M., Kourafalou, V.H., Paris, C.B., Helgers, J., Aman, Z.M., Hogan,
646 P.J., Srinivasan, A., 2012. Surface evolution of the Deepwater Horizon
647 oil spill patch: Combined effects of circulation and wind-induced drift.
648 Environmental Science & Technology 46, 7267–7273.
- 649 Lee, T.N., Leaman, K., Williams, E., Berger, T., Atkinson, L., 1995. Florida
650 Current meanders and gyre formation in the southern Straits of Florida.
651 Journal of Geophysical Research: Oceans 100, 8607–8620.
- 652 Lee, T.N., Mayer, D.A., 1977. Low-frequency current variability and spin-off
653 eddies along the shelf off southeast Florida. Collected Reprints 1, 344.
- 654 Lee, T.N., Smith, N., 2002. Volume transport variability through the Florida
655 Keys tidal channels. Continental Shelf Research 22, 1361–1377.
- 656 Lee, T.N., Williams, E., 1988. Wind-forced transport fluctuations of the
657 Florida Current. Journal of Physical Oceanography 18, 937–946.
- 658 Li, Z., Johns, B., 1998. A three-dimensional numerical model of surface
659 waves in the surf zone and longshore current generation over a plane beach.
660 Estuarine, Coastal and Shelf Science 47, 395–413.
- 661 Lin, N., Chavas, D., 2012. On hurricane parametric wind and applications in
662 storm surge modeling. Journal of Geophysical Research: Atmospheres 117.
- 663 Liu, Y., Weisberg, R.H., 2012. Seasonal variability on the West Florida shelf.
664 Progress in Oceanography 104, 80–98.
- 665 Liu, Y., Weisberg, R.H., Zheng, L., 2020. Impacts of hurricane Irma on the
666 circulation and transport in Florida Bay and the Charlotte Harbor estuary.
667 Estuaries and Coasts 43, 1194–1216.
- 668 Liubartseva, S., Coppini, G., Lecci, R., Clementi, E., 2018. Tracking plastics
669 in the Mediterranean: 2D Lagrangian model. Marine Pollution Bulletin
670 129, 151–162.

- 671 Longuet-Higgins, M.S., 1970. Longshore currents generated by obliquely
672 incident sea waves. *Journal of Geophysical Research* 75, 6778–6789.
- 673 Longuet-Higgins, M.S., Stewart, R., 1964. Radiation stresses in water waves;
674 a physical discussion, with applications, in: *Deep Sea Research and Oceanographic Abstracts*, Elsevier. pp. 529–562.
- 676 Lowe, R.J., Falter, J.L., Bandet, M.D., Pawlak, G., Atkinson, M.J., Moni-
677 smith, S.G., Koseff, J.R., 2005. Spectral wave dissipation over a barrier
678 reef. *Journal of Geophysical Research: Oceans* 110.
- 679 Madsen, O.S., Poon, Y.K., Gruber, H.C., 1989. Spectral wave attenuation by
680 bottom friction: Theory, in: *Coastal Engineering 1988*, pp. 492–504.
- 681 Malmstadt, J., Scheitlin, K., Elsner, J., 2009. Florida hurricanes and damage
682 costs. *Southeastern Geographer* 49, 108–131.
- 683 McWilliams, J.C., Restrepo, J.M., Lane, E.M., 2004. An asymptotic theory
684 for the interaction of waves and currents in coastal waters. *Journal of Fluid
685 Mechanics* 511, 135.
- 686 McWilliams, J.C., Sullivan, P.P., 2000. Vertical mixing by Langmuir circula-
687 tions. *Spill Science & Technology Bulletin* 6, 225–237.
- 688 Mei, C.C., 1989. The applied dynamics of ocean surface waves. volume 1.
689 World scientific.
- 690 Moon, I.J., Ginis, I., Hara, T., Thomas, B., 2007. A physics-based parame-
691 terization of air-sea momentum flux at high wind speeds and its impact on
692 hurricane intensity predictions. *Monthly Weather Review* 135, 2869–2878.
- 693 Pinelli, J.P., Roueche, D., Kijewski-Correa, T., Plaz, F., Prevatt, D., Zisis,
694 I., Elawady, A., Haan, F., Pei, S., Gurley, K., et al., 2018. Overview of
695 damage observed in regional construction during the passage of Hurricane
696 Irma over the State of Florida, in: *Forensic Engineering 2018: Forging*

- 697 Forensic Frontiers. American Society of Civil Engineers Reston, VA, pp.
698 1028–1038.
- 699 Powell, M.D., Houston, S.H., Amat, L.R., Morisseau-Leroy, N., 1998. The
700 HRD real-time hurricane wind analysis system. Journal of Wind Engineering
701 and Industrial Aerodynamics 77, 53–64.
- 702 Powell, M.D., Vickery, P.J., Reinhold, T.A., 2003. Reduced drag coefficient
703 for high wind speeds in tropical cyclones. Nature 422, 279–283.
- 704 Röhrs, J., Christensen, K.H., Hole, L.R., Broström, G., Drivdal, M., Sundby,
705 S., 2012. Observation-based evaluation of surface wave effects on currents
706 and trajectory forecasts. Ocean Dynamics 62, 1519–1533.
- 707 Schott, F.A., Lee, T.N., Zantopp, R., 1988. Variability of structure and
708 transport of the Florida Current in the period range of days to seasonal.
709 Journal of Physical Oceanography 18, 1209–1230.
- 710 Siadatmousavi, S.M., Jose, F., Stone, G., 2011. Evaluation of two WAM
711 white capping parameterizations using parallel unstructured SWAN with
712 application to the Northern Gulf of Mexico, USA. Applied Ocean Research
713 33, 23–30.
- 714 Sikirić, M.D., Roland, A., Janečković, I., Tomazić, I., Kuzmić, M., 2013.
715 Coupling of the Regional Ocean Modeling System (ROMS) and Wind
716 Wave Model. Ocean Modelling 72, 59–73.
- 717 Smith, N.P., 1982. Response of Florida Atlantic shelf waters to hurricane
718 David. Journal of Geophysical Research: Oceans 87, 2007–2016.
- 719 Spivakovskaya, D., Heemink, A., Milstein, G., Schoenmakers, J., 2005. Sim-
720 ulation of the transport of particles in coastal waters using forward and
721 reverse time diffusion. Advances in water resources 28, 927–938.

- 722 Stokes, G.G., 1880. On the theory of oscillatory waves. *Transactions of the*
723 *Cambridge Philosophical Society* .
- 724 Tolman, H.L., et al., 2009. User manual and system documentation of
725 WAVEWATCH III TM version 3.14. Technical note, MMAB Contribution
726 276, 220.
- 727 Van Den Bremer, T., Breivik, Ø., 2018. Stokes drift. *Philosophical Trans-*
728 *actions of the Royal Society A: Mathematical, Physical and Engineering*
729 *Sciences* 376, 20170104.
- 730 Villas Bôas, A.B., Cornuelle, B.D., Mazloff, M.R., Gille, S.T., Arduin, F.,
731 2020. Wave–current interactions at meso-and submesoscales: Insights from
732 idealized numerical simulations. *Journal of Physical Oceanography* 50,
733 3483–3500.
- 734 Wachnicka, A., Browder, J., Jackson, T., Louda, W., Kelble, C., Abdelrahman,
735 O., Stabenau, E., Avila, C., 2019. Hurricane Irmas impact on water quality
736 and phytoplankton communities in Biscayne Bay (Florida, USA). *Estuaries*
737 and Coasts , 1–18.
- 738 WAMDI Group, 1988. The WAM model – A third generation ocean wave
739 prediction model. *Journal of Physical Oceanography* 18, 1775–1810.
- 740 Weisberg, R., Liu, Y., Mayer, D., 2009. Mean circulation on the west Florida
741 continental shelf observed with long-term moorings. *Geophys. Res. Lett*
742 36, L19610.
- 743 Weisberg, R.H., Zheng, L., 2006. Hurricane storm surge simulations for
744 Tampa Bay. *Estuaries and Coasts* 29, 899–913.
- 745 Wu, L., Chen, C., Guo, P., Shi, M., Qi, J., Ge, J., 2011. A FVCOM-
746 based unstructured grid wave, current, sediment transport model, I. Model
747 description and validation. *Journal of Ocean University of China* 10, 1–8.

- 748 Xian, S., Feng, K., Lin, N., Marsooli, R., Chavas, D., Chen, J., Hatzikyriakou,
749 A., 2018. Brief communication: Rapid assessment of damaged residential
750 buildings in the Florida Keys after Hurricane Irma. *Natural Hazards and*
751 *Earth System Sciences* 18, 2041–2045.
- 752 Zedler, S., Niiler, P., Stammer, D., Terrill, E., Morzel, J., 2009. Ocean's
753 response to Hurricane Frances and its implications for drag coefficient
754 parameterization at high wind speeds. *Journal of Geophysical Research: Oceans* 114.
- 756 Zhang, C., Durgan, S.D., Lagomasino, D., 2019. Modeling risk of mangroves
757 to tropical cyclones: A case study of Hurricane Irma. *Estuarine, Coastal*
758 *and Shelf Science* 224, 108–116.